Journal of Loss Prevention in the Process Industries 83 (2023) 105050

Contents lists available at ScienceDirect

Journal of Loss Prevention in the Process Industries

journal homepage: www.elsevier.com/locate/jlp

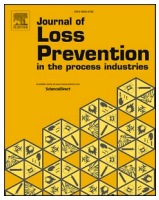

Numerical investigation of powder aerosolization in a mining rock dust dispersion chamber

Hongyu Chen [a], Leonid A. Turkevich [b,*], Milind A. Jog [a], Urmila Ghia [a]

[a] Thermal Fluids & Thermal Processing Lab, Mechanical & Materials Engineering, University of Cincinnati, Cincinnati, OH, 45221-0072, USA
[b] Division of Field Studies & Engineering (DFSE), National Institute for Occupational Safety & Health (NIOSH), The Centers for Disease Control & Prevention (CDC), Alice Hamilton Laboratory, 1090 Tusculum Avenue, Cincinnati, OH, 45226, USA

ARTICLE INFO

Keywords:
Dust dispersion
Dustiness
Explosion prevention
Euler-Lagrangian multiphase
RANS k-ω Turbulence

ABSTRACT

We have conducted numerical simulations of dust dispersion within the NIOSH Rock Dust Dispersion Chamber. The apparatus consists of a low-speed background ventilation flow down a long box in which is placed a tray containing a rock dust powder. A nozzle upstream of the tray introduces a short pulse of a turbulent horizontal jet flow just above the powder surface. We have utilized an incompressible Reynolds-Averaged Navier-Stokes k-ω model for the turbulent flow; particles are incorporated within a one-way Euler-Lagrangian formalism. The Rock Dust Dispersion Chamber ventilation flow exhibits a recirculation zone just above the powder-containing tray. Aerosolization proceeds via the interplay of the jet pulse flow with the background recirculation flow. The air flow is not well-mixed. The aerosolized dust is convected as a concentration cloud downstream towards the detection zone. For larger particles, gravitational settling depletes the convected cloud, so the instrument behaves as a horizontal elutriator. The instrument is robust with respect to misalignment of the jet nozzle. However, reduced streamwise drift velocity allows mixing to disperse the optically detected dust cloud concentration pulse. Our large particle simulation results compare favorably with published experimental results for large, polydisperse calcium carbonate rock dust.

1. Introduction

1.1. Dust

Dust consists of fine and ultrafine solid particles (typically formed by the physical disintegration of a parent material) that may become aerodynamically suspended (Kulkarni et al., 2011). Outdoor dust is typically generated by natural processes (e.g., aeolian or volcanic). In the workplace, airborne dust may be suspended by various processes like spills (Suter et al., 2010), pouring or transferring (Shaw et al. 1998; Chen et al., 2012; Cheng, 1973; Heitbrink et al., 1992), grinding or milling (Pensis et al., 2010).

1.1.1. Health effects of dust

Since the Renaissance (da Vinci, Paracelsus, Agricola), mine dust has been suspected of leading to adverse respiratory effects (Wallace and Hobbs, 2006; Kelly, 2008; Weber, 2002). Inhalation of industrial dust can lead to asbestosis (Brody, 1997), silicosis (Leung et al., 2012; Wagner, 1997; Weisman and Banks, 2003), byssinosis (Breum and Nielsen, 1996), agricultural pneumoconiosis (Schenker et al., 2009), and coal workers' pneumoconiosis (Castranova and Vallyathan, 2000). For recent reviews of the influence of dust on respiratory health, see Duffin et al., (2002, 2007), Sirajuddin & Kanne (2009), Donaldson & Seaton (2012) and Chen et al., 2021. Hence the accurate measurement of dust and its control is the subject of extensive interest (CEN 2006).

1.1.2. Explosion hazard of combustible dust

Combustible dust, when it accumulates on surfaces, may pose a potential explosion hazard. The National Fire Protection Association (NFPA) has established (NFPA, 2020) a critical depth criterion of 0.8 mm * [1200 kg/m^3]/ρ (where ρ is the bulk density of the dust), which, if exceeded poses a dust explosion hazard. The Association of German Engineers (Verein Deutscher Ingenieure—VDI) has a guideline (VDI 2263–9, 2008) to determine the dustiness of material directly related to dust explosion hazards.

1.1.3. Dustiness

Dustiness is 'the propensity of material to generate airborne dust

* Corresponding author.
E-mail address: LLT0@cdc.gov (L.A. Turkevich).

https://doi.org/10.1016/j.jlp.2023.105050
Received 1 September 2022; Received in revised form 13 December 2022; Accepted 30 March 2023
Available online 11 April 2023

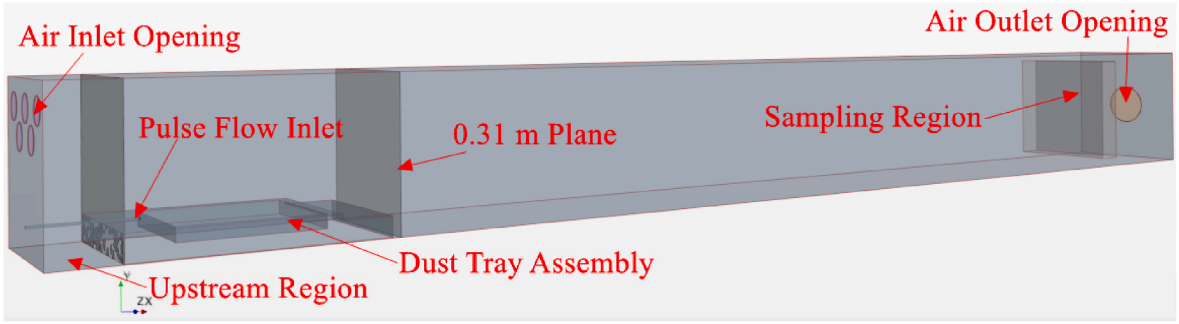

Fig. 1. Model of dust dispersion simulation: upstream region, 0.31 cm plane, sampling region.

during its handling' (Liden, 2006; Plinke et al., 1995). It is quantified by measuring that portion of a finely divided solid (a powder) that becomes airborne under a controlled mechanical or aerodynamic stimulus.

1.1.4. Dustiness testing methods

Various techniques have been developed for dustiness measurement (CEN, 2006; Davies et al., 1988; Kulkarni et al., 2011; Boundy et al., 2006; ISO, 2012; ASTM, 1980; DIN, 1999, 2006). The Venturi instrument has been used to test pharmaceutical powders (Boundy et al., 2006) and fine and ultrafine powders (Evans et al., 2013). The rotating drum and continuous drop test methods are included in the European Standard EN15051 (CEN, 2006) to determine the dustiness in a workplace environment. Schneider & Jensen (2008) used a smaller Danish drum for dustiness testing. The Australian standard rotating drum is used for dustiness measurements of bulk solids (Standards Australia, 2013; Wypych & Mar 1988). The German Standard Heubach dustmeter (DIN, 2006) has been widely used for occupational dustiness determination (Heitbrink, Todd, Cooper & O'Brien, 1990).

All of these techniques explore the aerosolization of bulk powders. However, the aerosolization of a dust layer from surfaces is extremely important yet has received limited investigation. Lee et al., (2019) studied particle resuspension from dusty surfaces by spinning the substrate in a centrifuge; orientation of the substrate relative to the centrifugal radius permits a separate estimate of normal (lift) and tangential resuspension forces. These experiments focus on particle depletion from the substrate rather than on their aerosolization. The NIOSH rock dust dispersion chamber (Perera et al., 2016) addresses the aerodynamic generation of a dust cloud from a dusty surface.

1.1.5. Numerical modeling of dustiness testing

In an effort to evaluate different dustiness testing procedures, we have initiated a research program using Computational Fluid Dynamics (CFD) to model various dusting apparatuses. Dubey et al., 2017) used CFD to investigate the injection into and sampling within the Venturi dustiness tester. The aerosolization process within the Venturi injection tube has also been investigated using CFD (Palakurthi, 2017; Sharma et al., 2020a, 2020b; Palakurthi et al., 2022). CFD is also a common tool in rotating drum dustiness tester research. Yang et al., 2008) used CFD to investigate the flow regimes of bulk solids in a rotating drum. (Wangchai et al., 2013, 2015, 2016), Wangchai (2017) and Ilic et al., 2016 used CFD-DEM to investigate the aggregation characteristic of bulk solids tumbling in rotating drum dustiness testers. Chen2021) used CFD to study the dynamic range and instrument function of the EN15051 and Danish drums. A similar study (Chen et al., 2023) was conducted on the smaller, rapidly rotating Heubach drum.

The present study is a first step towards predicting the dispersion of particles from dust lying on a surface. Simplifications have been made. The results of the present simulation are directly compared with tests performed with the NIOSH Dust Dispersibility Chamber (section 1.2.3).

1.2. Dustiness from surfaces—importance for mine hazards

1.2.1. Dust explosion in mines

Coal dust explosions typically occur when a mixture of flammable

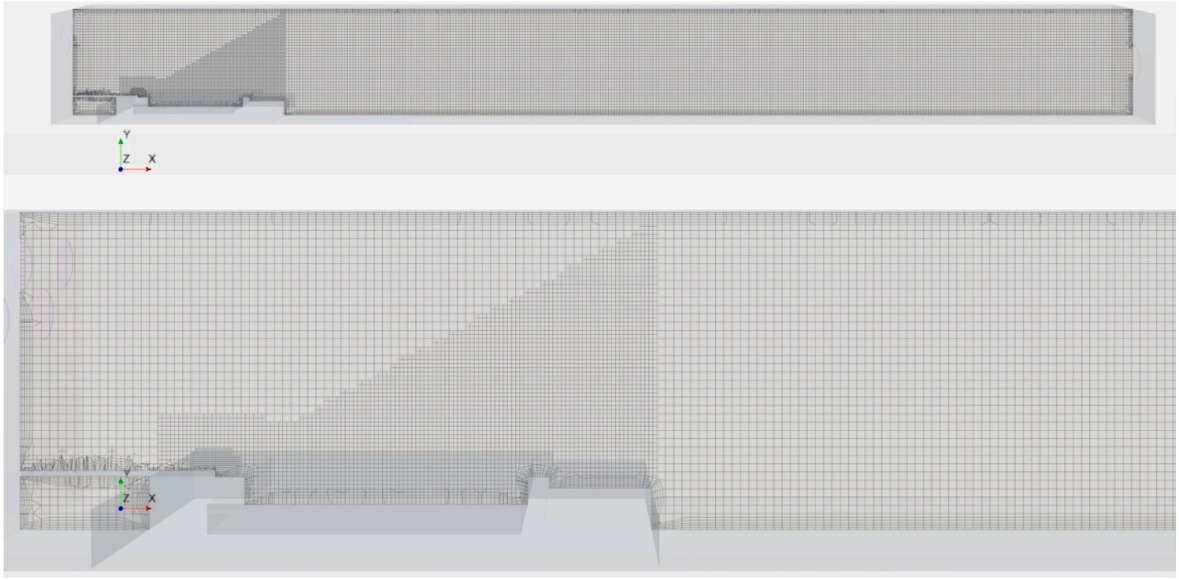

Fig. 2. Mesh of dust dispersibility simulation.

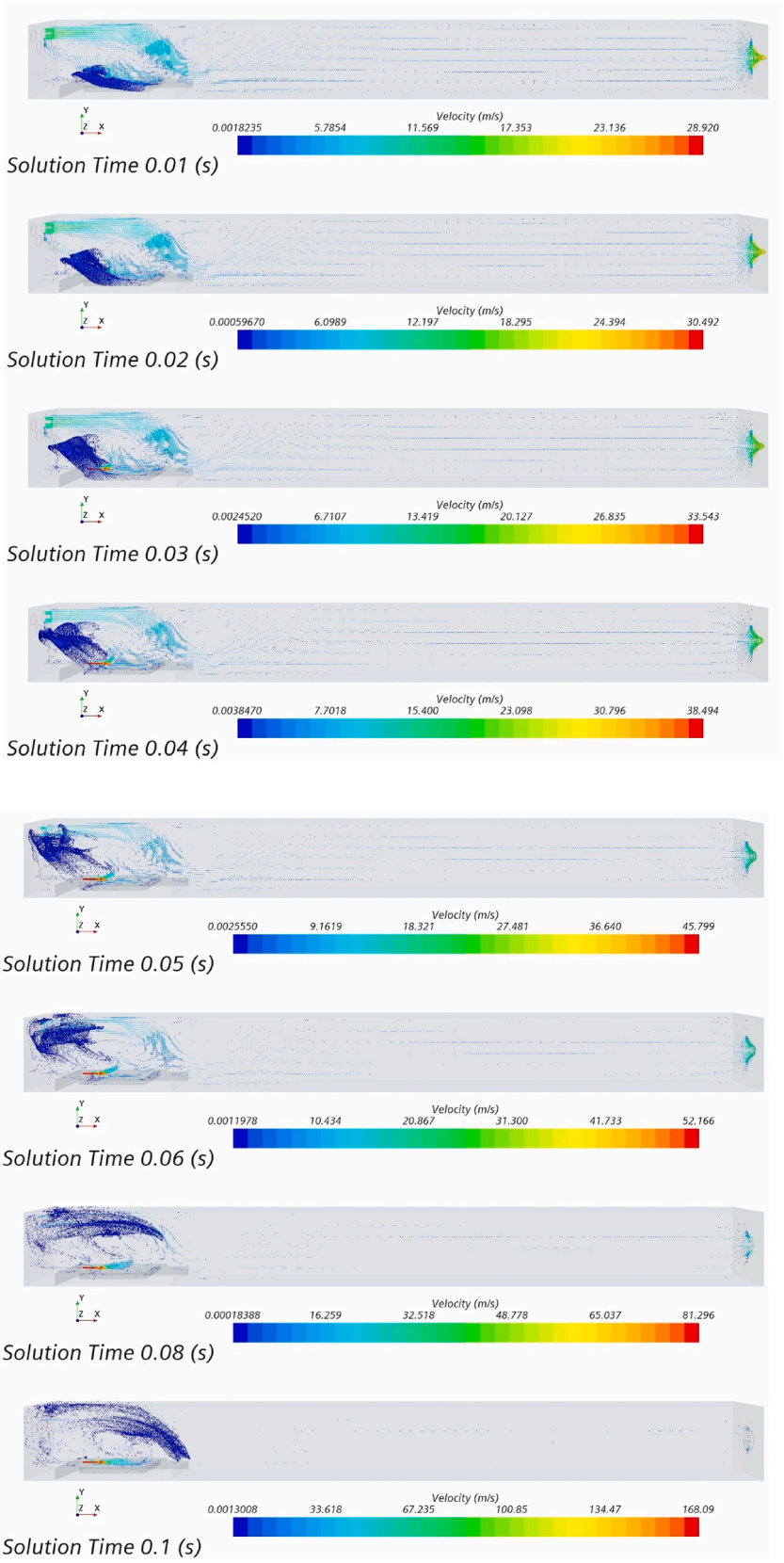

Fig. 3. Side view of the dispersing of 1 μm particles. Particle locations (throughout the domain) in dark blue; color map of velocity magnitude in central axial plane. Times: 0.01, 0.02, 0.03, 0.04, 0.05, 0.06, 0.08, 0.1, 0.25, 0.5, 0.75, 1 s. (For interpretation of the references to color in this figure legend, the reader is referred to the Web version of this article.)

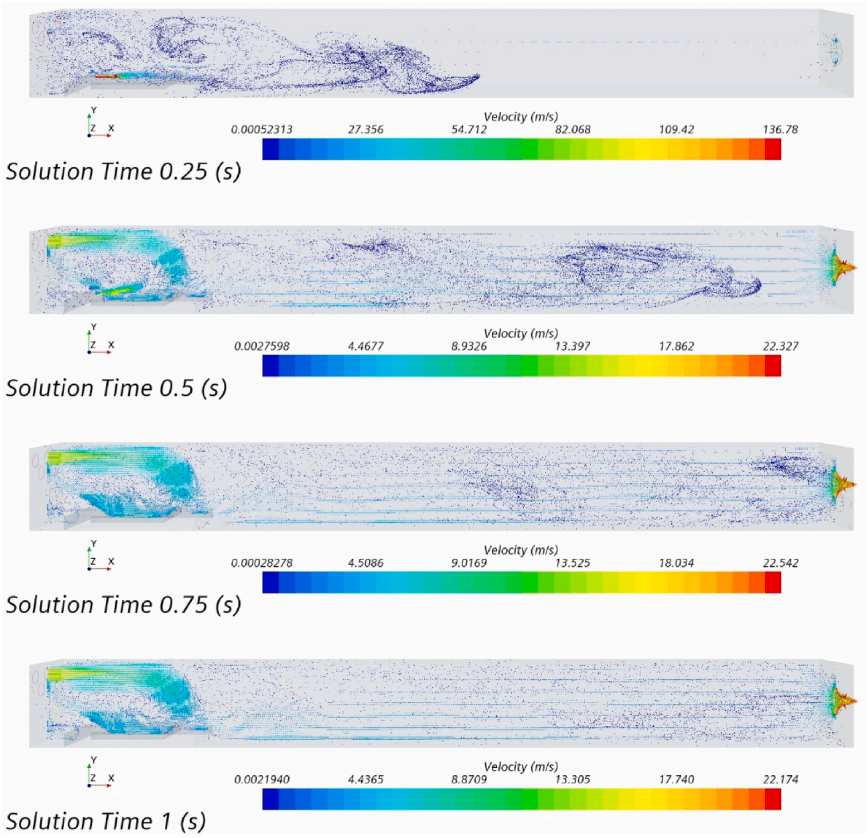

Fig. 3. (*continued*).

methane and air is ignited in the presence of coal dust. The rapidly expanding high temperature gases create a pressure wave, that may steepen into a shock wave as it progresses away from the ignition source. The wind from the shock wave disperses dust from any exposed surfaces (roof, walls, floor). The resulting dust cloud is ignited by the propagating flame front produced by the initial methane explosion. Repeated cycles of this process may generate multiple dust explosions downstream from the initial ignition site. A crucial precondition for such explosions to occur is an extensive surface layer of combustible dust.

1.2.2. Rock dusting in mines

The application of dispersible rock dust (typically, pulverized limestone) is a widely used technique to inert coal dust explosions and prevent continued flame propagation (Hartman et al., 1954; Cybulski, 1975; Sapko et al., 1987a, b, 1998; NIOSH, 2011; Harris et al., 2015). It is believed that the rock dust absorbs both thermal and radiant energy from the heated and combusting gases, thereby reducing the preheating of unburned coal particles ahead of the flame front.

Greenwald (1938), Dawes (1952a, b), Dawes & Wynn (1952), and Cybulski (1975) conducted experiments to characterize the dispersibility relevant to preventing dust explosions. NIOSH developed (Perera et al., 2016) the rock dust dispersion chamber to study the dispersibility of rock dusts for use as a screening device for candidate inerting materials. Earlier work (Rice et al., 1927; BOM, 1960) utilized a light brush stroke or a gentle air puff (as from the mouth) as the dispersing impetus. The NIOSH rock dust dispersion chamber standardized the blast of air to correspond to realistic winds encountered in mine explosions (Perera et al., 2016).

1.2.3. NIOSH rock dust dispersion tester

A schematic of the NIOSH rock dust dispersion chamber is provided in Fig. 1, which details the domain of our simulations. The NIOSH dispersion chamber is a 15.24 cm (6 in) high, 15.24 cm (6 in) wide, 152.4 cm (60 in) long clear methacrylate plastic box (Perera et al., 2016). A pressure difference of $\Delta p = 370$ Pa (between the five entrance holes upstream and the single exit hole downstream) establishes a ventilation flow of 1.52 m/s down the length of the chamber; the ventilation exchange time is thus $t_{exch} = 1$ s (For comparison, a lower pressure drop of $\Delta p = 75$ Pa establishes a ventilation flow of 0.67 m/s, with an exchange time of $t_{exch} = 2.27$ s; these are the conditions of our grid-convergence simulations reported in Section 3.7.)

A uniform layer of dust is added to a dust tray (outside dimensions: 14.5 cm wide, 19.25 cm long, 2.54 cm deep), which has a front ledge (4.6 cm long, 14.5 cm wide). The inside cavity, which contains the dust is 13.6 cm long, 12.3 cm wide, 1.34 cm deep. The depth of the dust layer is experimentally 1.3 cm (1/2 in). Experimentally (Perera et al., section 2.1), the tray is loaded by gently spooning the powder into the tray, with the excess (powder above the surface of the tray) removed by the horizontal sliding of a knife across the tray surface. There is no tamping down of the powder, which is thus not compressed. For the simulations, a monolayer of particles is placed at the top plane of the dust tray cavity. The tray is pre- and post-weighed to obtain a gravimetric measure of the fraction of dust dispersed. In our simulations, the entire monolayer of dust is always aerosolized.

Test samples are subjected to a standardized (triangular-shaped) 0.3 s air pulse from a compressed air reservoir. This air pulse is intended to mimic the winds generated during typical mine dust explosions (Cashdollar et al., 2010; NIOSH 2011), both in the time-integrated dynamic pressure and in the peak dynamic pressure of 0.29 bar (4.2 psi). The air pulse emerges from a stainless-steel tube (OD = 0.32 cm = 1/8 in, ID = 0.14 cm–0.06 in), with the exit hole positioned 3,2 cm (1.25 in) from the leading edge of the dust layer, and parallel to the top of the dust layer.

Experimentally, an optical dust probe is positioned downstream (Fig. 1 'Sampling Region' 129.5 cm from the exit of the nozzle and 13.5 cm from the chamber exit); obscuration results from the dispersed

Fig. 4. Top view of the dispersing of 1 μm particles. Particle locations (throughout the domain) in dark blue. Times: 0.01, 0.02, 0.03, 0.04, 0.05, 0.06, 0.08, 0.1, 0.25, 0.5, 0.75, 1 s. (For interpretation of the references to color in this figure legend, the reader is referred to the Web version of this article.)

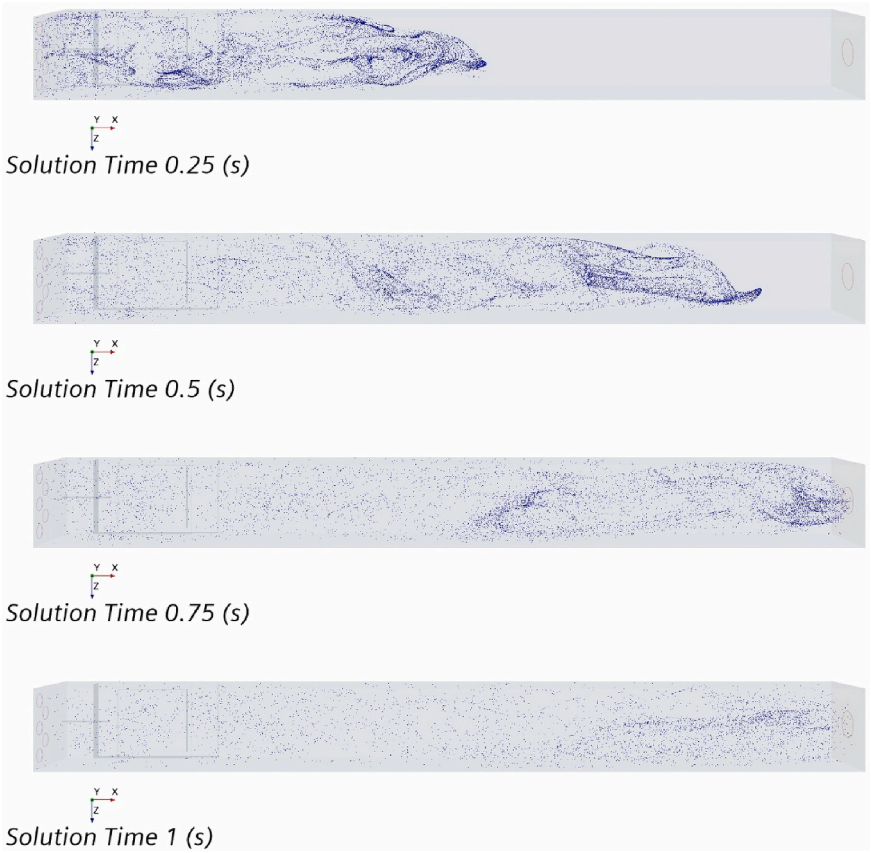

Fig. 4. (*continued*).

dust cloud being convected downstream. The optical obscuration is proportional to the dust concentration in the optical path of the probe. In the simulation, we measure the dust concentration in a 1 cm slab, located at 129 cm downstream of the nozzle exit.

2. Numerical methods

2.1. Grid generation

Structured grids were generated within STAR-CCM+; cells are cubes ('trimmed cells') in the bulk of the domain and flattened rectangular prisms at the boundary surfaces. A trimmed cell mesh (base cell size = 4.0 mm) was generated in the simulation domain with refinement in the boundary and pulse flow regions, as shown in Fig. 2. Boundary layers are refined by 5 layers of prism cells with a growth factor of 1.1. Wake refinement is used (up to 21 cm) downstream of the pulse injection; the spread angle of the wake refinement region is 30°.

For grid verification, additional meshes with base sizes of 3.0 mm, 5.0 mm, 6.0 mm were generated. These grid verification meshes used the same refinement recipe as the 4.0 mm mesh.

2.2. Numerical simulation method

2.2.1. Air flow only

With a drift air flow of $u_{drift} = 1.52$ m/s, the Reynolds number is $Re_{drift} \sim 1.6 * 10^4$. When the jet is turned on, the maximum dynamic pressure, $p_{max} = 0.29$ bar, corresponds to a velocity of $u_{jet} \sim 200$ m/s. Emerging from the jet nozzle (d = 0.3175 cm), this corresponds to $Re_{nozzle} \sim 4.7 * 10^4$, but this jet sets up flow in the larger dust chamber corresponding to $Re_{jet/box} \sim 2 * 10^6$.

The CFD simulations were conducted in two stages. Initially, the drift flow is established with a steady-state simulation; after the drift flow has converged, the model is switched to transient. Both stages were conducted using incompressible Reynolds-Averaged Navier-Stokes equations with a Shear-Stress *k-ω* turbulence model (Menter 1994, 2009; Wilcox, 2006). The equations were solved numerically using the finite-volume pressure-based solver, STAR-CCM+. The convection terms are discretized using a second-order upwind scheme. The discretized governing equations are solved using the SIMPLE (Semi-Implicit Method for Pressure-Linked Equations) algorithm for pressure-velocity coupling (Patankar, 1980). Velocity and pressure under-relaxation factors are 0.9 and 0.5, respectively. For the second, time-dependent URANS (Unsteady Reynolds-Averaged Navier-Stokes) stage, the temporal discretization is second-order implicit. The time step is set at $\Delta t = 2.5 * 10^{-4}$ s; the simulation is run for T = 3 s. The solution of the equations was considered to be converged when the scaled residuals for the continuity and momentum equations decreased to 10^{-5} for each time step.

The URANS k-ω turbulence treatment was previously used (Dubey et al., 2017) to model the jet flow in the Venturi Dustiness Tester.

2.2.2. Justification of incompressible air model

In the NIOSH rock dust dispersion chamber, the highest pulse flow velocity is 200 m/s, corresponding to a local Mach number of M = 0.61. Wang & Andreopoulos (2003) have studied the spatial evolution of the centerline velocity for turbulent, subsonic jets, issuing into still air. They find that, for nitrogen, at M = 0.6, by a distance x/D ~15, the centerline velocity has decayed to half of its initial value (i.e., M ~ 0.3). The diameter of the NIOSH jet nozzle is 1.4 mm, so by 2.1 cm, the flow is effectively incompressible, and this is still 1.1 cm shy of the tray depression, where the dust particles are located. This estimate thus supports our assumption of incompressibility for this study.

2.2.3. Addition of particles—particle tracking—one way coupling

Once the drift flow is established, spherical silica ($\rho = 2500$ kg/m^3)

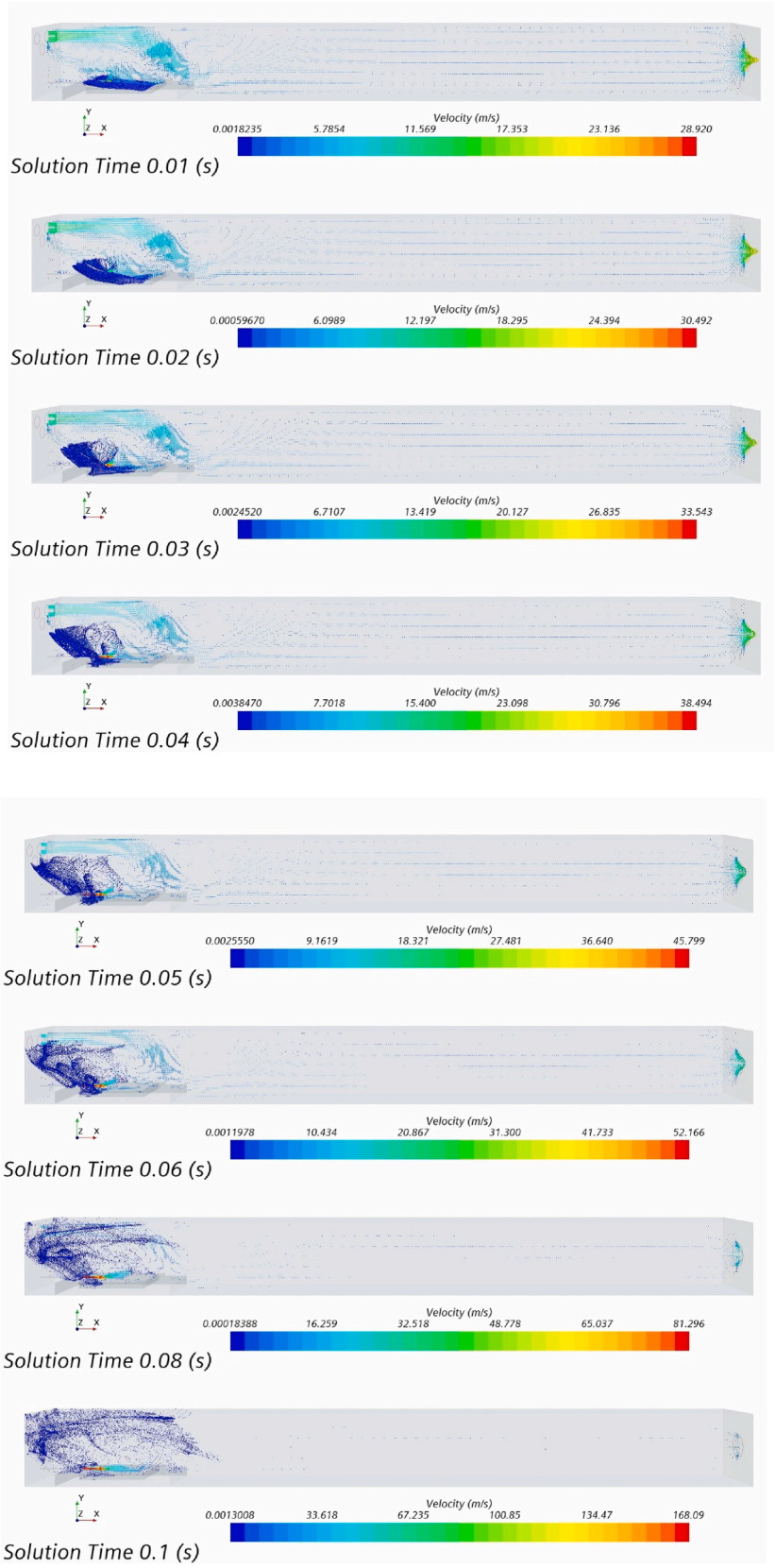

Fig. 5. Side view of the dispersing of 50 μm particles. Particle locations (throughout the domain) in dark blue; color map of velocity magnitude in central axial plane. Times: 0.01, 0.02, 0.03, 0.04, 0.05, 0.06, 0.08, 0.1, 0.25, 0.5, 0.75, 1 s. (For interpretation of the references to color in this figure legend, the reader is referred to the Web version of this article.)

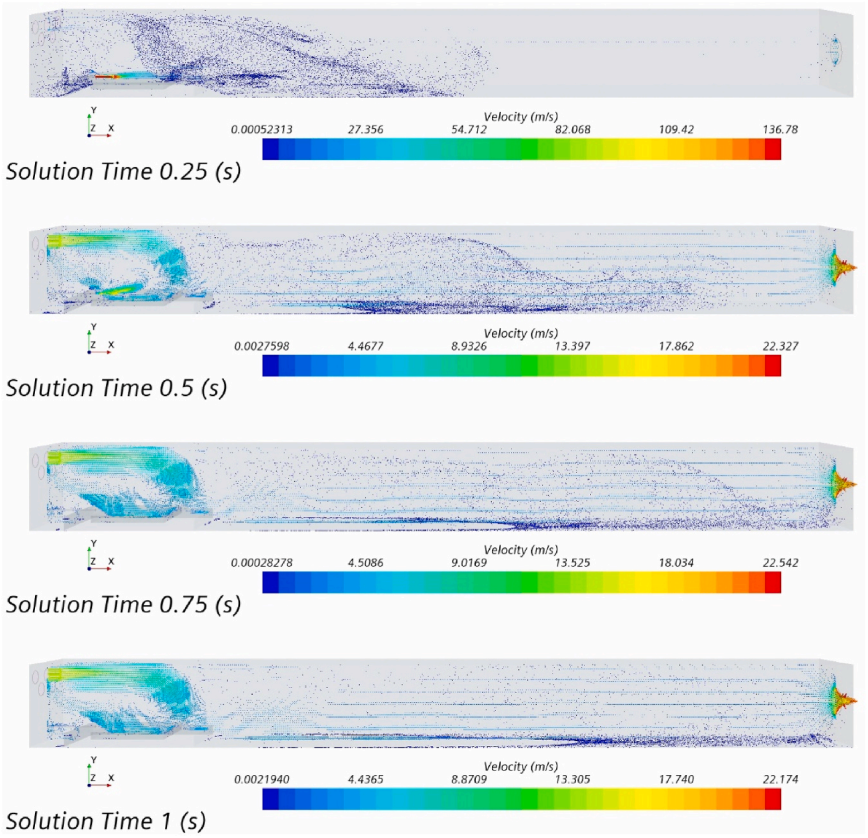

Fig. 5. (*continued*).

particles (N = 16,605) are injected from rest at t = 0 (using the STAR-CCM + Parcel Injector), distributed uniformly on a plane at ledge height in the tray cavity. Tracking of particles is incorporated via the Euler-Lagrangian Method with one-way coupling between the air continuum and the particles; coupling includes Stokes (viscous) drag, Saffman lift and gravitational forces; rotation of the particles is not included, so there is no Magnus force. For the largest particles ($D_p = 100\,\mu m$), the volume fraction occupied in the tray region is $\phi \sim 10^{-5}$. Particle-particle interactions are neglected; thus, these simulations cannot address the very real effect of moisture on inerting rock dusts. Particle agglomeration and break-up are also neglected since aerodynamic shear forces are insufficient to break up agglomerates; while particle impact on chamber walls may induce break-up, this has been neglected. Particle-wall interaction is modeled as pure elastic collision (i.e., unit coefficient of restitution), so no particles stick to the chamber walls.

3. Results and discussion

Figs. 3 and 4 show a time sequence of particle locations and flow velocity magnitude for side and top views for the simulation with 1 μm particles. In the side view (Fig. 3), the particles are shown throughout the domain; the magnitude of the flow velocity (color map) is shown on a vertical plane bisecting the dust chamber down its center. In the top view (Fig. 4), only the particles are shown throughout the domain. We discuss these pictures in the following sections.

3.1. Air flow characteristics

We first discuss the air flow in these experiments. This can be seen in the velocity color map of Fig. 3 (focus on the air flow colormap and ignore the particles in these figures).

The steady-state background drift flow consists of overall axial flow down the dust dispersion chamber. At the early time (t = 0.01 s) and late times (t > 0.5 s), there is no jet flow (color map velocity maximum ~ 22 m/s). The inflow (central top entrance hole) and outflow (single exit hole) are apparent. However, this particular geometry (5 inlet holes at the top of the chamber) supports a recirculation zone above the tray. This can be seen in the early time (t = 0.01 s) and late time (t = 1.0 s) light blue upstream velocity color maps of Fig. 3. Note that the recirculation occurs for the background drift, both before and after the dispersing jet. (Recirculation persists during the jet flow but is not evident in the figures due to the change in velocity scale to accommodate the higher jet velocity.) Similar recirculation occurs for flow over a backward-facing step (Armaly et al., 1983; Durst and Tropea, 1983; Adams and Eaton, 1988; Jovic and Driver, 1994; Le et al., 1997; Zajec et al., 2021). Once the jet is turned on, the velocity scale increases (velocity maximum ~ 168 m/s at t = 0.1 s); the jet is apparent, but because of the change in velocity scale, the inflow and outflow are no longer resolved in this figure. Aerosolization of the particles in the tray results from the interplay of the jet flow with the recirculation zone. If it is desired to study dust dispersion purely from the action of the jet flow, the apparatus will need to be modified, most easily by moving the dust tray downstream of the recirculation zone, i.e., by at least 30 cm.

3.2. Particle trajectories

We now turn to the behavior of the dust particles. At early times (t = 0.01 s), while the jet is still ramping up, the recirculation zone pulls back the dust layer and lofts it up towards the upstream (inlet) wall. At t = 0.03 s, the jet protrudes through the dust layer. At t = 0.04 s, the dust layer encounters the upstream (inlet) wall, and at t = 0.05 s it reaches the junction of the upstream (inlet) wall and ceiling. At t = 0.08 s, the dust cloud is in the upper third of the chamber over the tray; the jet is blowing into clear air. At t = 0.1 s, the dust cloud is pulled down towards

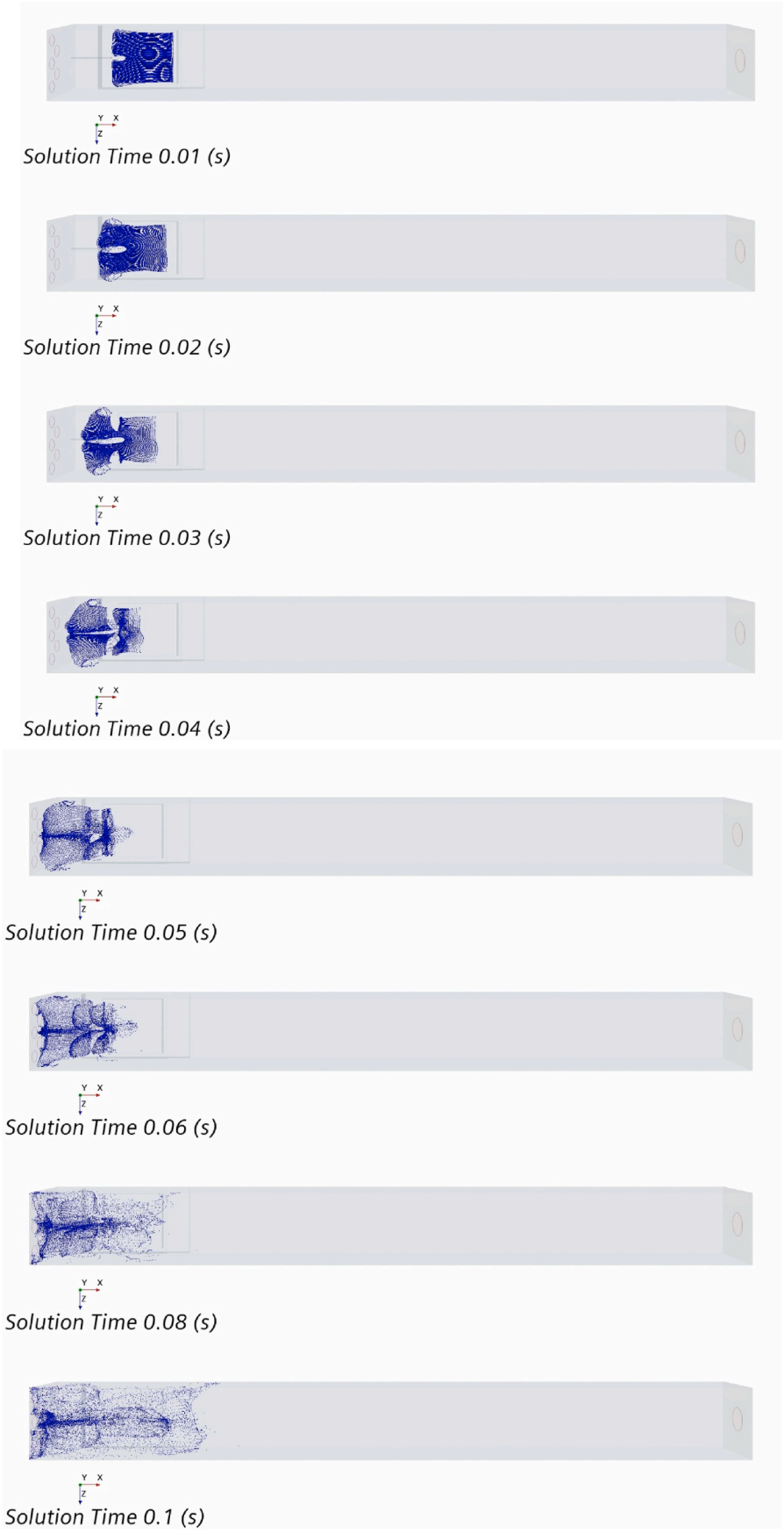

Fig. 6. Top view of the dispersing of 50 μm particles. Particle locations (throughout the domain) in dark blue. Times: 0.01, 0.02, 0.03, 0.04, 0.05, 0.06, 0.08, 0.1, 0.25, 0.5, 0.75, 1 s. (For interpretation of the references to color in this figure legend, the reader is referred to the Web version of this article.)

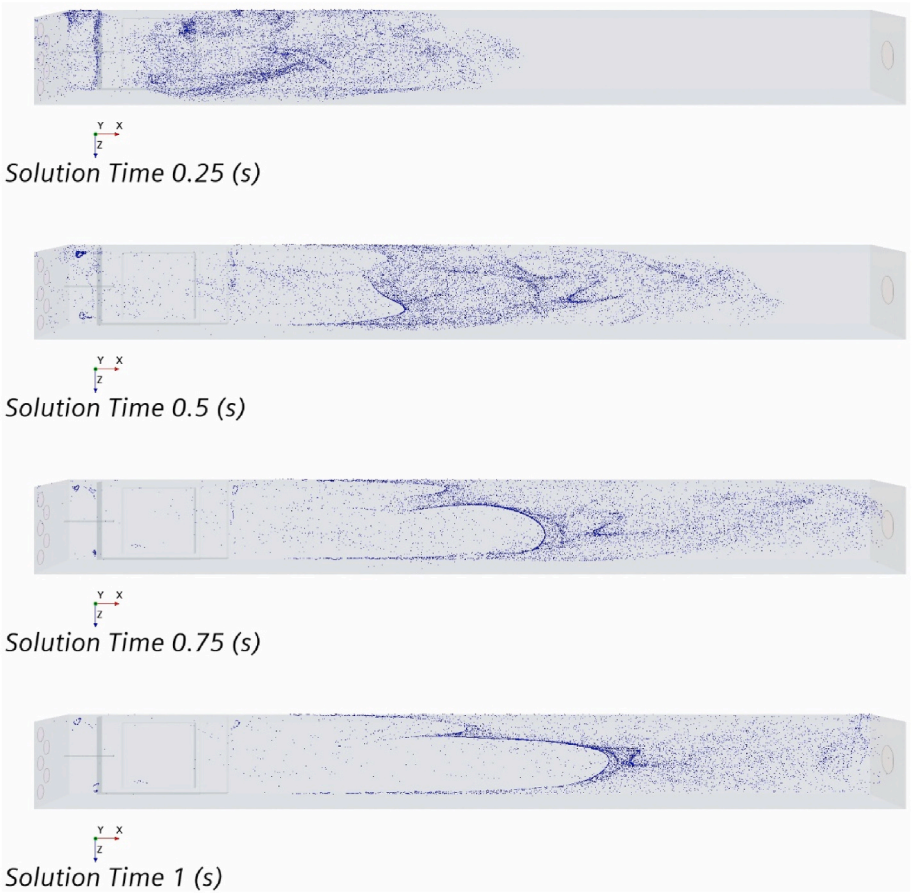

Fig. 6. (*continued*).

the downstream end of the tray. At t = 0.25 s, the dust cloud occupies the upstream half of the chamber; at t = 0.5 s, the dust cloud is dispersed throughout the chamber, with the leading edge in the detection zone; at t = 0.75 s, the dust cloud occupies the last sixth of the chamber. However, throughout (and this is very apparent at t = 1.00 s), a fraction of the dust particles continues to recirculate in the volume above the dust tray.

The top view sequence (Fig. 4) provides another perspective on the dynamics of the dust layer. At small times (t < 0.05 s), the dust layer is pulled upstream (by the recirculation). As the jet is turned on, a region in front of the jet is cleared of particles (already evident at t = 0.01 s). By t = 0.06 s, the layer has rolled up to the top surface and is propelled forward. The front is spanwise well-defined and uniform at t = 0.1 s but becomes less well-defined as it is convected downstream (t > 0.25 s).

Combining side and top perspectives, for t < 0.1 s, the dust layer remains essentially intact as it is pulled upstream and up and then rolls forward. For t > 0.1 s, the dust roll becomes dispersed into a volume, which is convected downstream, with the preponderance of particles at the leading edge of the convecting dust cloud. We also note that the dust cloud is never uniformly distributed throughout the domain, as would be the case for a well-mixed system. By contrast, at the lower drift velocity (pictures not shown), mixing becomes more competitive, and the dust cloud is dispersed before the detection zone (section 3.6.2).

3.3. Particle size effects

We have conducted similar simulations with varying particle sizes. The behavior for 10 μm particles is indistinguishable from that of the 1 μm particles. However, differences in particle dispersion become apparent at the larger particle sizes. Figs. 5 and 6 show similar side and top panel views for 50 μm particles. The recirculation is less effective at drawing up the layer of particles (already evident at t = 0.05 s); the downstream edge of the dust layer remains inertially stable. For 0.05 s < t < 0.1 s, the 1 μm particle layer remains intact, but the 50 μm particles already are dispersed throughout the volume above the dust tray. As the dust cloud is convected downstream, gravitational settling becomes apparent for t > 0.25 s. The rock dust dispersion chamber essentially acts as a horizontal elutriator. In the Supplemental Material we have provided side view videos for a sequence of simulations for multiple particle sizes: 0.1, 0.5, 1, 5, 10, 15, 20, 25, 30, 35, 40, 45, 50, 55, 60, 65, 70, 75, 80, 100 μm. As the particle size increases, particles settle over time, so the rock dust dispersion chamber acts as a horizontal elutriator.

3.4. Particle detection downstream

Experimentally, dust is detected downstream by optical obscuration (proportional to the particle concentration, although the cross-section varies with particle size and material index of refraction). We have simulated this measurement by calculating the particle concentration in a volume at this location. This is shown (curve in magenta, scale at right) in the sequence of Fig. 7. For comparison, the jet flow is shown (curve in red, scale at left). Also shown (curve in green) is the experimental optical detection (Perera et al., 2016) of large polydisperse calcium carbonate rock dust (the peak has been normalized to correspond to the maximum of the simulated peak in each panel). The magnitude of the detected dust cloud pulse is relatively constant until d = 25 μm, whereupon it drops precipitously. The onset of particle detection is relatively invariant (at

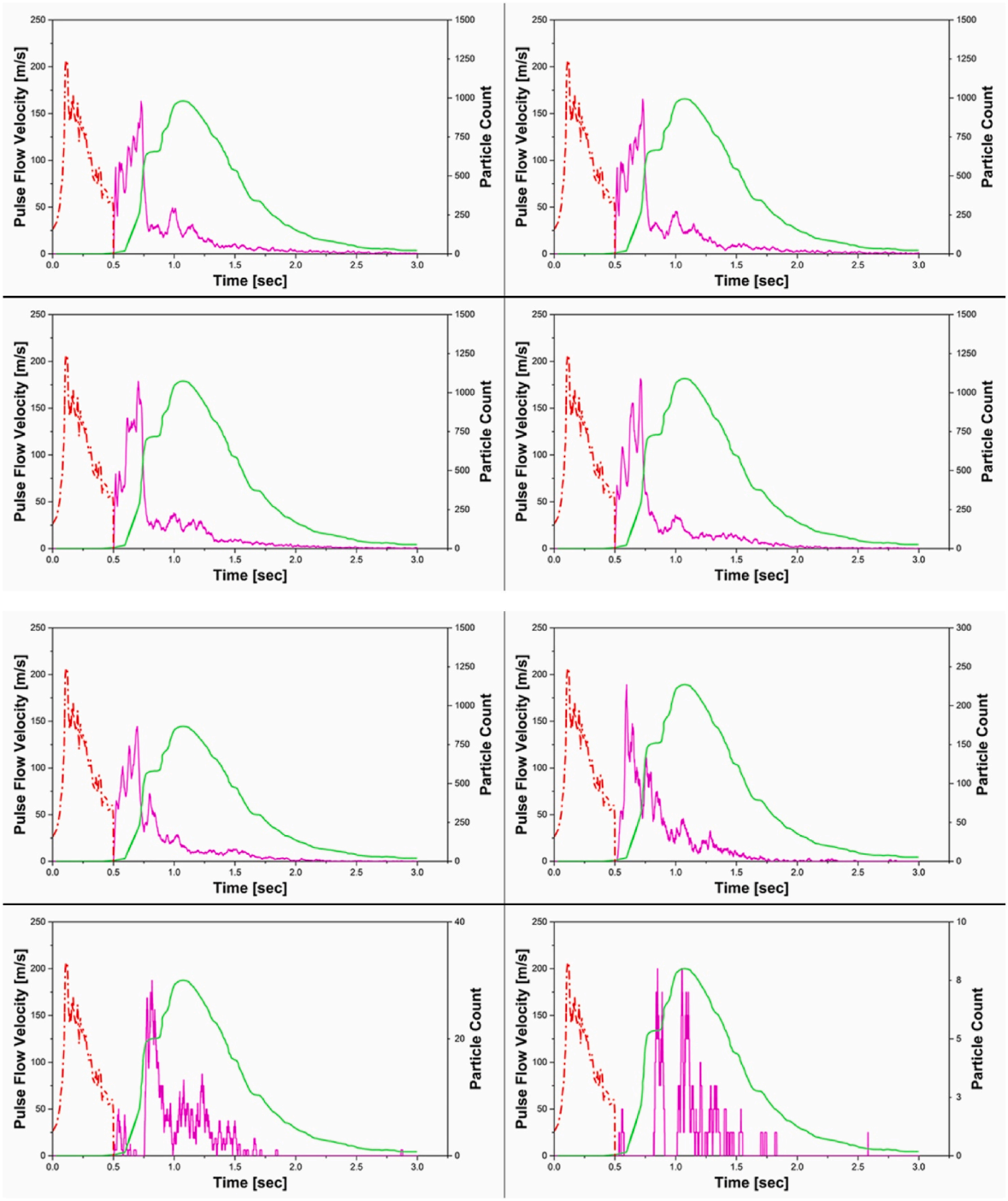

Fig. 7. Sampled particle count (magenta curve—scale at right), pressure difference = 370 Pa, aligned pulse flow, particle sizes: 100 nm, 1 μm, 5 μm, 15 μm, 25 μm, 50 μm, 75 μm, 100 μm. Time profile of velocity at nozzle (red curve—scale at left). Experimental optically detected signal from large polydisperse calcium carbonate rock dust (peak normalized green curve). (For interpretation of the references to color in this figure legend, the reader is referred to the Web version of this article.)

t = 0.5 s) with particle size until d = 50 μm, and thereafter is increasingly delayed. The detected dust cloud pulse is narrow in arrival time, with a long, delayed tail; at the higher particle sizes, this delayed tail represents a larger fraction of the detected dust cloud pulse (but, of course, the overall signal decreases with particle size).

For comparison, we have shown the experimentally detected optical pulse (Perera et al., 2016) of large, polydisperse calcium carbonate rock dust; the size distribution of this material is bimodal, with comparable overlapping peaks centered at 10 μm and 100 μm. This detected pulse is clearly broader than any of our simulated pulses. Because the optical extinction scales with the particle cross-section, $\sigma \sim D_p^2$, the experimental signal is dominated by the larger particles in the distribution. We thus believe that the experimental results are consistent with the 100 μm simulations.

Our comparison (Fig. 7) has been made with the large polydisperse calcium carbonate reference rock dust of Perera et al. (2016). These authors have studied the effect of moisture on this rock dust; moisture induces significant caking, rendering the rock dust undispersible. Stearate and hydrophobic spray treatment prevents caking; the spray-treated rock dust is dispersible, even after exposure to water. It is remarkable

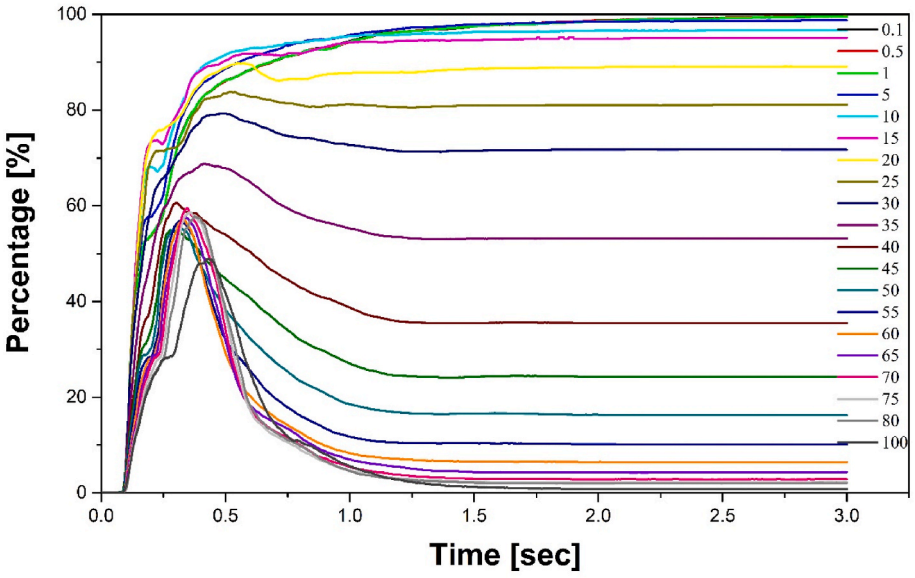

Fig. 8. Variation of total dustiness with particle size; pressure difference = 370 Pa, aligned pulse flow.

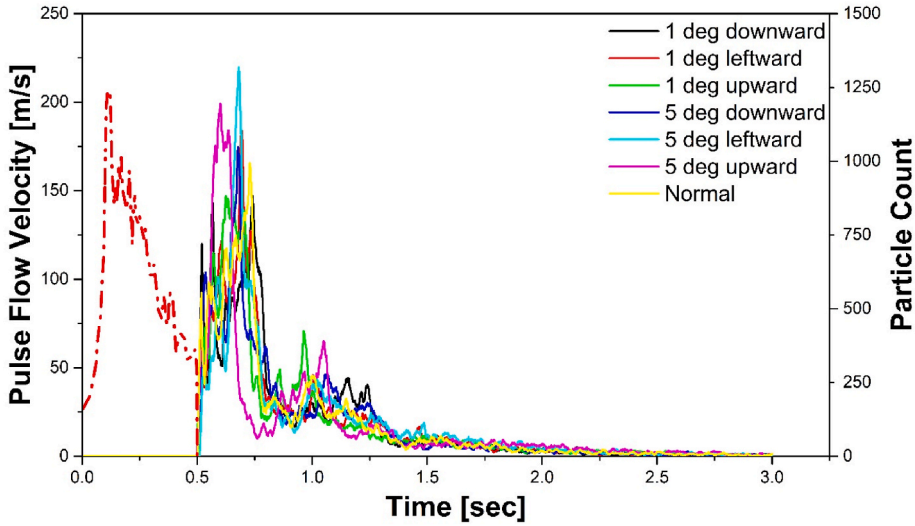

Fig. 9. Comparison of sampled particle count (scale at right) for different pulse flow inlet angles; 370 Pa background pressure. Time profile of velocity at nozzle (dashed red curve—scale at left). (For interpretation of the references to color in this figure legend, the reader is referred to the Web version of this article.)

that the dust profile shape scales (Perera et al., Fig. 9 and discussion in section 3.1) for these three dusts (reference, spray-treated dry, spray-treated wet, with peaks in the ratios 3.4:15.2:6.7). In the light of our simulations, this is understood as reflecting a particle size distribution unchanged by spray treatment, with differing source strengths resulting from the different dispersibilites of the three powders.

3.5. Dustiness

In these simulations, all the particles are lofted from the dust tray; this corresponds to a material dustiness of unity (no cohesive interactions have been included in the simulations). As a practical matter, in order to better characterize this instrument, we define the total measured dustiness as the fraction of particles that are transported downstream of the dust tray (plane at x = 31 cm) and which remain above h = 5 mm from the floor of the chamber. Fig. 8 displays the total dustiness as a function of time for different particle sizes. Note that this definition includes the fraction of particles that are transported out of the chamber through the downstream exit hole. For the larger particle sizes, gravitational settling becomes increasingly important, thereby making evident the behavior of the rock dust chamber as a horizontal elutriator.

3.6. Instrument parameter sensitivity

We now examine the sensitivity of this instrument to changes in two of the operating parameters: jet misalignment, and reduced ventilation flow.

3.6.1. Jet nozzle direction

We first examine the sensitivity to small misalignments of the jet nozzle direction with respect to the chamber axis. Fig. 9 displays the concentration in the detection zone for 1 μm particles, where i) the jet nozzle is properly aligned (in the axial direction); ii) misaligned by 1° downward, to the left, upward; iii) misaligned by 5° downward, to the left, upward. There is no significant change in the detected dust pulse.

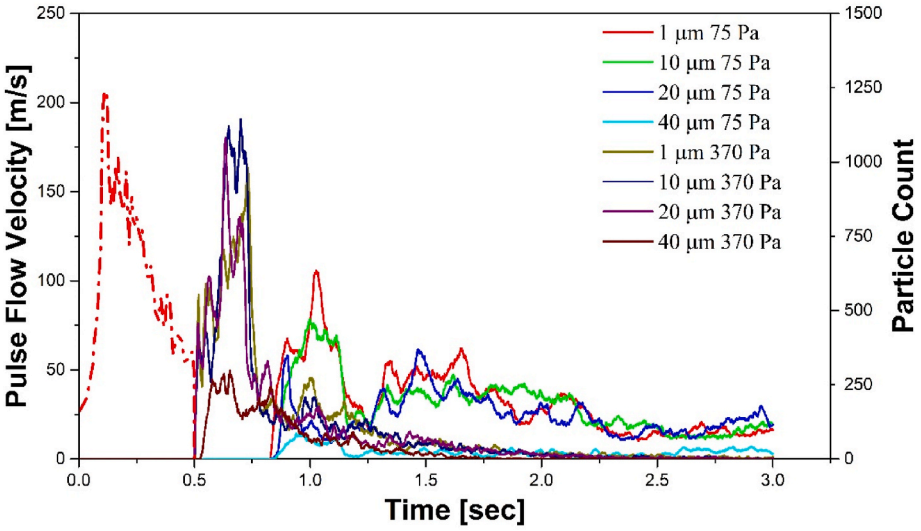

Fig. 10. Sampled particle count–comparison between 75 and 370 Pa (scale at right). Time profile of velocity at nozzle (dashed red curve—scale at left). (For interpretation of the references to color in this figure legend, the reader is referred to the Web version of this article.)

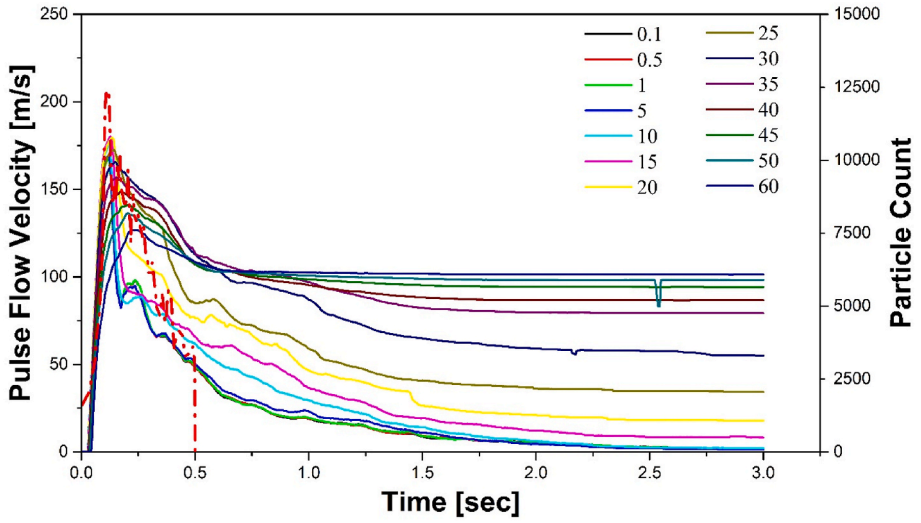

Fig. 11. Upstream particle fraction (scale at right), pressure difference = 75 Pa, aligned pulse flow, particles sizes given in μm. Time profile of velocity at nozzle (dashed red curve—scale at left). (For interpretation of the references to color in this figure legend, the reader is referred to the Web version of this article.)

Surprisingly, the rock dust dispersion instrument is remarkably robust to small misalignments of the dispersing jet.

3.6.2. *Reduced chamber flow*

We next examine the sensitivity to the drift flow velocity. While we have not examined this parameter in detail, we have conducted a set of simulations at reduced drift velocity in order to probe whether control of this parameter is important. Fig. 10 displays the detected dust pulse for 0.1, 1, 10, 20, 40, 60 μm particles a) at the standard operating drift velocity ($u_{drift} = 1.52$ m/s set up with a pressure difference of 370 Pa), and b) at a significantly reduced drift velocity ($u_{drift} = 0.67$ m/s set up with a pressure difference of 75 Pa). For the reduced drift velocity, the particle count in the dust cloud pulse is significantly reduced, and its shape is significantly broadened.

We attribute both effects to upstream trapping of lofted particles in the recirculation zone above the dust tray, which are then inefficiently swept downstream by the reduced drift velocity. Fig. 11 displays the sizeable fraction of particles remaining in the region upstream of the dust tray for the reduced drift velocity simulations. This should be contrasted (Fig. 12) with the reduced fraction of particles remaining in the region upstream of the dust tray under standard operating drift velocity conditions.

3.7. *Grid independence verification*

In order to estimate the sensitivity of our simulation results to the discrete size of the grid (Celik et al., 2008), we have conducted simulations (without particles) on additional grids, with base sizes of 6 mm and 3 mm. We have monitored the steady-state air mass flow rate (in the absence of the aerosolizing jet) for the reduced pressure drop $\Delta p = 75$ Pa: $Q_3 = 18.51455$ g/s (for the 3 mm grid), $Q_4 = 18.52817$ g/s (for the 4 mm grid), $Q_6 = 18.56208$ g/s (for the 6 mm grid); in the limit of zero grid size, the infinitely refined grid possesses the (unknown) mass flow rate Q_0. Assuming (Richardson scaling (Richardson, 1910)) that the error in the measured quantity (air mass flow rate Q) scales as a power, p, of the grid size, $Q_h - Q_0 = \alpha\, h^p$. The scaling exponent, p, may be extracted from the algebraic relation, $(Q_6\text{-}Q_4)/(Q_4\text{-}Q_3) = (6^p - 4^p)/(4^p - 3^p)$; we obtain $p = 1.6162$. Hence, for our calculations on the

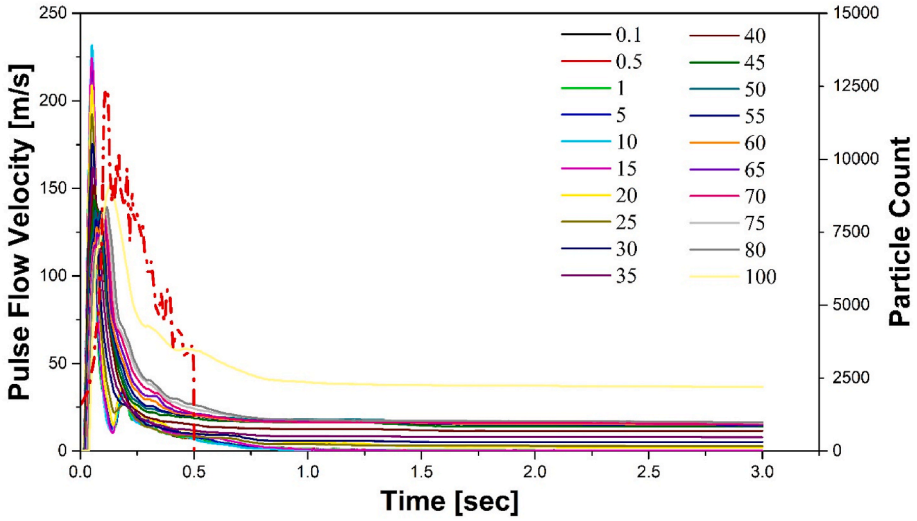

Fig. 12. Upstream particle fraction (scale at right), pressure difference = 370 Pa, aligned pulse flow, particle sizes given in μm. Time profile of velocity at nozzle (dashed red curve—scale at left). (For interpretation of the references to color in this figure legend, the reader is referred to the Web version of this article.)

4 mm grid, the relative error in the mass flow rate is an acceptable 0.198%.

4. Conclusion

We have conducted CFD simulations of dust dispersion within the NIOSH Rock Dust Dispersion Chamber. The apparatus consists of a uniform background ventilation flow down a long box; a nozzle introduces a short ($\Delta t \sim 0.3$ s) jet pulse parallel to, and just above, the surface of a tray containing powder.

We have utilized an incompressible Reynolds-Averaged Navier-Stokes k-ω model for the turbulent flow within the Rock Dust Dispersion Chamber; particles are incorporated within a one-way Euler-Lagrangian formalism.

The Rock Dust Dispersion Chamber ventilation flow exhibits a recirculation zone just above the powder-containing tray. Aerosolization proceeds via the interplay of the jet flow from the nozzle with the background recirculation flow. If it is desired to study dust dispersion solely from the action of the jet nozzle flow, we recommend repositioning the dust-containing tray downstream by at least 30 cm (i.e., downstream of the ventilation flow recirculation zone); we also recommend supplemental CFD simulations to model this revised configuration.

The air flow is not well-mixed. The aerosolized dust cloud is convected downstream to the detection zone. The lack of mixing ensures that a dust cloud pulse is detected downstream. For larger particles, gravitational settling depletes this pulse as it is convected downstream, so the NIOSH Rock Dust Dispersion Chamber behaves as a horizontal elutriator.

The instrument is robust with respect to misalignment of the jet nozzle. However, the background drift velocity appears to be an important parameter that needs to be controlled; with reduced drift velocity, mixing broadens and decreases the optically detected concentration pulse.

Our large particle ($D_p = 100$ μm) simulated concentration pulse compares favorably with the experimentally measured optical pulse from large, polydisperse (modes at 10 μm and 100 μm) calcium carbonate rock dust (Perera et al., 2016).

We have also conducted a grid convergence study (with grids of base sizes 3, 4, 6 mm). The error in steady-state mass flow rate varies with grid size, h, as $Q_h - Q_0 \sim h^p$, with $p = 1.6162$. The relative error in mass flow rate, using the 4 mm grid (as we have done for our dispersion simulations) is 0.198%.

Disclaimer

The findings and conclusions of this paper are those of the authors and do not necessarily represent the views of the National Institute for Occupational Safety and Health, Centers for Disease Control and Prevention. Mention of any product or company name does not constitute endorsement by the National Institute for Occupational Safety and Health, Centers for Disease Control and Prevention. None of the authors has a financial relationship with a commercial entity that has an interest in the subject of this paper.

Co-author responsibilities for rock dust dispersion chamber paper

Hongyu Chen performed the CFD simulations. Milind A. Jog and Urmila Ghia provided guidance for the CFD simulations. Leonid Turkevich formulated the simulation problem, directed the project and wrote the manuscript.

Declaration of competing interest

The authors declare that they have no known competing financial interests or personal relationships that could have appeared to influence the work reported in this paper.

Data availability

No data was used for the research described in the article.

Acknowledgments

We thank J. Bennett and D.E. Evans (both of NIOSH) for helpful discussions. This work is supported, in part, by the NIOSH Nanotechnology Research Center (NTRC).

Appendix A. Supplementary data

Supplementary data to this article can be found online at https://doi.org/10.1016/j.jlp.2023.105050.

References

Adams, E.W., Eaton, J.K., 1988. An LDA study of the backward-facing step flow, including the effect of velocity bias. J. Fluid Eng. 110, 275–282.

Armaly, B.F., Durst, F., Pereira, J.C.F., Schoenung, B., 1983. Experimental and theoretical investigation of backward-facing step flow. J. Fluid Mech. 127, 473–496.

ASTM, 1980. Standard Test Method for Index of Dustiness of Coal and Coke, vol. 26. ASTM standards. ANSI/ASTM D-547-41.

BOM, 1960. American standard practice for rock dusting underground bituminous-coal and lignite mines to prevent coal-dust explosion. In: (ASA Standard M13.1-1960, UDC 622.81). US Dept. of the Interior, US Bureau of Mines, Information Circular 8001.

Boundy, M., Leith, D., Polton, T., 2006. Method to evaluate the dustiness of pharmaceutical powders. Ann. Occup. Hyg. 50, 453–458.

Breum, N.O., Nielsen, E.M., 1996. Dust content of cotton—quality control in terms of airborne dust and endotoxin: a pilot study. Gefahrst. Reinhalt. Luft 56 (10), 389–392.

Brody, A.R., 1997. Asbestosis. In: Roth, R.A. (Ed.), Comprehensive Toxicology, vol. 8. Elsevier Science, New York, pp. 393–413.

Cashdollar, K.L., Sapko, M.J., Weiss, E.S., Harris, M.L., Man, C.K., Harteis, S.P., Green, G. M., 2010. *Recommendations for a New Rock Dusting Standard to Prevent Coal Dust Explosions in Intake Airways* (Report of Investigations 9679). US Dept. of Health & Human Services, Centers for Disease Control & Prevention, National Institute for Occupational Safety & Health, DHHS (NIOSH), Publication. No 2010-151.

Castranova, V., Vallyathan, V., 2000. Silicosis and coal workers' pneumoconiosis. Environ. Health Perspect. 108 (Suppl. 4), 675–684.

Celik, I.B., Ghia, U., Roache, P.J., Freitas, C.J., Coleman, H., Raad, P.E., 2008. Procedure for estimation and reporting of uncertainty due to discretization in CFD applications. J. Fluid Eng. 130, 078001.

CEN, 2006. Workplace Atmospheres—Measurement of the Dustiness of Bulk Materials—Requirements and Reference Test Methods.

Chen, H., Jog, M.A., Evans, D.E., Turkevich, L.A., 2021. Numerical investigation of powder aerosolization in a rotating drum apparatus. Powder Technol. 390, 62–72.

Chen, H., Jog, M.A., Turkevich, L.A., 2023. Computational fluid dynamics simulations of aerosol behavior in a high-speed (Heubach) rotating drum dustiness tester. Particuology 72C, 68–80.

Chen, X., Wheeler, C., Donohue, T., McLean, R., Roberts, A., 2012. Evaluation of dust emissions from conveyor transfer chutes using experimental and CFD simulation. Int. J. Miner. Process. 110, 101–108.

Cheng, L., 1973. Formation of airborne respirable dust at belt conveyor transfer points. Am. Ind. Hyg. Assoc. J. 34, 540–546.

Cybulski, W.G., 1975. Coal Dust Explosions and Their Suppression (Translated from Polish). National Center for Scientific, Technical and Economic Information, Warsaw, POL. NTIS No. TT 73-54001.

Davies, K., Hammond, C., Higman, R., Wells, A., 1988. Progress in dustiness estimation: British occupational hygiene society technology committee working party on dustiness estimation. Ann. Occup. Hyg. 32, 535–544.

Dawes, J.C., 1952a. Dispersion of dust deposits by blasts of air—part 1. Saf. Mine. Res. Establ. (U.K.) Res. report 36.

Dawes, J.C., 1952b. Dispersion of dust deposits by blasts of air—part 2. Saf. Mine. Res. Establ. (U.K.) Res. report 49.

Dawes, J.C., Wynn, A.H.A., 1952. The dispersion of dust by blast. Saf. Mine. Res. Establ. (U.K.) Res. report 46.

DIN, 1999. Determination of a parameter for the dust formation of pigments and extenders—part 2: drop method, p. 6. DIN 55992-2.

DIN, 2006. Determination of a parameter for the dust formation of pigments and extenders—part 1: rotation method, p. 8. DIN 55992-1.

Donaldson, K., Seaton, A., 2012. A short history of the toxicology of inhaled particles. Part. Fibre Toxicol. 9, 13.

Dubey, P., Ghia, U., Turkevich, L.A., 2017. Computational fluid dynamics analysis of the Venturi dustiness tester. Powder Technol. 312, 310–320.

Duffin, R., Tran, C.L., Clouter, A., Brown, D.M., MacNee, W., Stone, V., Donaldson, K., 2002. The importance of surface area and specific reactivity in the acute pulmonary inflammatory response to particles. Ann. Occup. Hyg. 46, 242–245.

Duffin, R., Tran, L., Brown, D., Stone, V., Donaldson, K., 2007. Proinflammogenic effects of low toxicity and metal nanoparticles *in vivo* and *in vitro*: highlighting the role of particle surface area and surface reactivity. Inhal. Toxicol. 19, 849–856.

Durst, F., Tropea, C., 1983. Flows over two-dimensional backward-facing steps. In: Dumas, R., Fulachier, L. (Eds.), Structure of Complex Turbulent Shear Flow, Int. Union of Theoretical & Applied Mechanics (IUTAM) Conference. Springer, Berlin & Heidelberg, pp. 41–52, 1983.

Evans, D.E., Turkevich, L.A., Roettgers, C.T., Deye, G.J., Baron, P.A., 2013. Dustiness of fine and nanoscale powders. Ann. Occup. Hyg. 57, 261–277.

Greenwald, H.P., 1938. Recent Trends in Rock Dusting to Prevent Dust Explosions in Coal Mines. American Institute of Mining & Metallurgical Engineers meeting (October 1938, Chicago, IL), Technical publication No. 975.

Harris, M.L., Sapko, M.J., Zlochower, I.A., Perera, I.E., Weiss, E.S., 2015. Particle size and surface area effects on explosibility using a 20-L chamber. J. Loss Prev. Process. Ind. 37, 33–38.

Hartman, H., Nagy, J., Rauschenberger, M.D., 1954. Coal-mine-explosion Research 1954-1955. US Dept. of the Interior, Bureau of Mines, RI 5264, Pittsburgh, PA.

Heitbrink, W.A., Baron, P.A., Willeke, K., 1992. An investigation of dust generation by free falling powders. Am. Ind. Hyg. Assoc. J. 53, 617-, 624.

Heitbrink, W.A., Todd, W.F., Cooper, T.C., O'Brien, D.M., 1990. The application of dustiness tests to the prediction of worker dust exposure. Am. Ind. Hyg. Assoc. J. 51, 217–223.

Ilic, D., Planner, J., Biswas, S., Reid, S., 2016. Revision of AS 4156.6—coal preparation—part 6: determination of dust/moisture relationship for coal. In: ICBMH 2016 Conf. Proceedings (12th International Conf. On Bulk Materials Storage, Handling and Transportation).

ISO, 2012. Nanomaterials—quantification of Nano-Object Release from Powders by Generation of Aerosols. ISO/TS 12025.

Jovic, S., Driver, D.M., 1994. Background-facing step measurements at low Reynolds number, Reh = 5000. NASA Technical Memorandum 108807.

Kelly, E., 2008. Paracelsus the innovator: a challenge to Galenism from 'On the miner's sickness and other miner's diseases. Univ. Western Ontario Medical J. 78, 70–74.

Kulkarni, P., Baron, P.A., Willeke, K., 2011. Introduction of aerosol characterization (chapter 1). In: Kulkarni, P., Baron, P.A., Willeke, K. (Eds.), Aerosol Measurement Principles, Techniques and Applications. John Wiley & sons, Hoboken, N.J., p. 5, 2011.

Le, H., Moin, P., Kim, J., 1997. Direct numerical simulation of the turbulent flow over a backward-facing step. J. Fluid Mech. 330, 349–374.

Lee, H.H., Cheung, Y.S., Fu, S.C., Chao, C.Y.H., 2019. Study of particle resuspension from dusty surfaces using a centrifugal method. Indoor Air 29, 791–802.

Leung, C.C., Yu, I.T.S., Chen, W., 2012. Silicosis. *Lancet* 379, 2008–2018.

Liden, G., 2006. Dustiness testing of materials handled at workplaces. Ann. Occup. Hyg. 50, 437–439.

Menter, F.R., 1994. Two-equation eddy-viscosity turbulence models for engineering applications. AIAA J. 32, 1598–1605.

Menter, F.R., 2009. Review of the shear-stress transport turbulence model–experience from an industrial perspective. Int. J. Comput. Fluid Dynam. 23, 305–316.

NFPA, 2020. National Fire Protection Association (NFPA) 654. *Standard for the Prevention of Fire and Dust Explosions from the Manufacturing, Processing, and Handling of Combustible Particulate Solids, Section*, 7.2.

NIOSH, 2011. Non-conforming Rock Dust. US Dept. of Health & Human Services. Centers fir Disease Control & Prevention, National Institute for Occupational Safety & Health, DHHS (NIOSH) Publication No. HID 16.

Palakurthi, N.K., 2017. Aerodynamics of Particle Detachment from Surfaces: a Numerical Study. M.Sc. thesis. Univ. Cincinnati, Dept. of Mechanical & Materials Engineering.

Palakurthi, N.K., Ghia, U., Turkevich, L.A., 2022. Numerical investigation of aerosolization in the Venturi dustiness tester: aerodynamics of a particle on a hill. J. Fluid Eng. 144 (6), 061113.

Patankar, S.V., 1980. Numerical Heat Transfer and Fluid Flow. Hemisphere Publishing Corp., McGraw-Hill, Washington, DC, 1980.

Pensis, I., Mareels, J., Dahmann, D., Mark, D., 2010. Comparative evaluation of the dustiness of industrial minerals according to European standard EN 15051, 2006. Ann. Occup. Hyg. 54, 204–216.

Perera, I.E., Sapko, M.J., Harris, M.L., Zlochower, I.A., Weiss, E.S., 2016. Design and development of a dust dispersion chamber to quantify the dispersibility of rock dust. J. Loss Prev. Process. Ind. 39, 7–16.

Plinke, M.A.E., Leith, D., Boundy, M.G., Loeffler, F., 1995. Dust generation from handling powders in industry. Am. Ind. Hyg. Assoc. J. 56, 251–257.

Rice, G.S., Paul, J.W., Greenwald, H.P., 1927. Coal-dust explosion tests in the experimental mine 1919 to 1924, inclusive. US Dept. of Commerce, Bureau of Mines, Bulletin 268.

Richardson, L.F., 1910. The approximate arithmetical solution by finitedifferences of physical problems involving differential equations, with an application to the stresses in a masonry dam. Philos. Trans. R. Soc. London, Ser. A 210, 307–357.

Sapko, M.J., Hertzberg, M., Watson, R.W., Cashdollar, K.L., 1987a. Dust explosion size scaling. In: Proc. Shenyang Int. Symp. On Dust Explosions. Shenyang, China, pp. 271–287 (Shenyang, China, 14-16 September 1987).

Sapko, M.J., Weiss, E.S., Watson, R.W., 1987b. Explosibility of float coal dust distributed over a coal-rock dust substratum. In: Proc. 22nd Int. Conf. Of Safety in Mines Research Institutes, pp. 459–468. Beijing, China, 2-6 November 1987.

Sapko, M.J., Weiss, E.S., Cashdollar, K.L., Zlochower, I.A., 1998. Experimental mine and laboratory dust explosion research at NIOSH. In: Proc. Int. Symp. On Hazards, Prevention and Mitigation of Industrial Explosions: 8th Int. Colloquium on Dust Explosions. Safety Consulting Engineers, Schaumburg, IL, pp. 120–142. -25 September 1998).

Schenker, M.B., Pinkerton, K.E., Mitchell, D., Vallyathan, V., Elvine-Kreis, B., Green, F.H. Y., 2009. Pneumoconiosis from agricultural dust exposure among young California farmworkers. Environ. Health Perspect. 117, 988–994.

Schneider, T., Jensen, K.A., 2008. Combined single drop and rotating drum dustiness test of fine to nanosize powders using a small drum. Ann. Occup. Hyg. 52, 23–34.

Sharma, A., Ghia, U., Turkevich, L.A., 2020a. Effect of vortex shedding on the aerosolization of a particle from a hill using large eddy simulation. In: Proceedings of the 2020 AIAA Aviation Forum. June 2020), paper 339120.

Sharma, A., Ghia, U., Turkevich, L.A., 2020b. Large eddy simulation of flow over a hemispherical obstacle within a cylindrical tube. In: Proceedings of the ASME 2020 Fluids Engineering Division Science Meeting FEDSM2020 (July 2020) paper 10596.

Shaw, B.W., Buharivala, P.P., Parnell Jr., C.B., Denny, M.A., 1998. Emission factors for grain receiving and feed loading operations at feed mills. Trans. ASAE (Am. Soc. Agric. Eng.) 41, 757–765.

Sirajuddin, A., Kanne, J.P., 2009. Occupational lung disease. J. Thorac. Imag. 24, 310.

Standards Australia, 2013. Coal Preparation—Part 6: Determination of Dust/moisture Relationship for Coal. AS4156.6.

Suter, S.L., Johnston, J.W., Mishima, J., 2010. Investigation of accident-generated aerosols: releases from free-fall spills. Am. Ind. Hyg. Assoc. J. 43, 540–543.

VDI 2263-9, 2008. Verein Deutscher Ingenieure. *Dust fires and Dust Explosions—Hazards—Assessment—Protective Measures—Determination of Dustiness of Bulk Materials*.

Wagner, G.R., 1997. Asbestosis and silicosis. Lancet 349, 1311–1315.

Wallace, J.M., Hobbs, P.V., 2006. Atmospheric Science: an Introductory Survey, second ed. Elsevier, Amsterdam. 2006.
Wang, Z., Andreopoulos, Y., 2003. Compressibility effects in turbulent subsonic jets. In: Proceedings of FEDSM'03 4th ASME, JSME Joint Fluids Engineering Conference (6-10 July 2003. Honolulu, HI, pp. FEDSM2003–45079.
Wangchai, S., 2017. Experimental and Numerical Investigations of Particle/air Flows in Dustiness Testers. Ph.D. thesis. Univ. Wollongong, Dept. of Mechanical, Materials, Mechatronic & Biomedical Engineering.
Wangchai, S., Hastie, D.B., Wypych, P.W., 2013. The simulation of particle flow mechanisms in dustiness testers. In: 11th International Conf. On Bulk Materials Storage. Handling and Transportation.
Wangchai, S., Hastie, D.B., Wypych, P.W., 2015. The investigation of particle flow mechanisms of bulk materials in dustiness testers. Part. Sci. Technol. 34, 241–254.
Wangchai, S., Hastie, D.B., Wypych, P.W., 2016. Particle size segregation of bulk material in dustiness testers via DEM simulation. Part. Sci. Technol. 36, 20–28.
Weber, L.W., 2002. Georgius Agricola (1494-1555): scholar, physician, scientist, entrepreneur, diplomat. Toxicol. Sci. 69, 292–294.
Weisman, D.N., Banks, D.E., 2003. Silicosis and coal worker's pneumoconiosis. In: Schwarz, M.J., King Jr., T.E. (Eds.), Interstitial Lung Disease, fourth ed. Decker, Inc., Hamilton, BC, pp. 391–416. 2003.
Wilcox, D.C., 2006. Turbulence Modeling for CFD, third ed. DCW Industries, Inc., La Canada, CA. 2006.
Wypych, P., Mar, L., 1988. Investigations into the dustiness of bulk materials. Aust. Bulk Handl. Rev. 18, 64–67.
Yang, R., Yu, A., McElroy, L., Bao, J., 2008. Numerical simulation of particle dynamics in different flow regimes in a rotating drum. Powder Technol. 188, 170–177.
Zajec, B., Matkovic, M., Kosanic, N., Oder, J., Mikuz, B., Kren, J., Tiselj, I., 2021. Turbulent flow over confined backward-facing step: PIV vs. DNS. Appl. Sci. 11, 10582.